

# Chemical Science

Accepted Manuscript

This article can be cited before page numbers have been issued, to do this please use: J. Wu, J. Sun, T. Liang, Y. Zhang, H. Zhang, T. Zhang, X. Feng, P. Gao, P. Xu and J. Li, *Chem. Sci.*, 2026, DOI: 10.1039/D5SC08898D.



This is an Accepted Manuscript, which has been through the Royal Society of Chemistry peer review process and has been accepted for publication.

Accepted Manuscripts are published online shortly after acceptance, before technical editing, formatting and proof reading. Using this free service, authors can make their results available to the community, in citable form, before we publish the edited article. We will replace this Accepted Manuscript with the edited and formatted Advance Article as soon as it is available.

You can find more information about Accepted Manuscripts in the [Information for Authors](#).

Please note that technical editing may introduce minor changes to the text and/or graphics, which may alter content. The journal's standard [Terms & Conditions](#) and the [Ethical guidelines](#) still apply. In no event shall the Royal Society of Chemistry be held responsible for any errors or omissions in this Accepted Manuscript or any consequences arising from the use of any information it contains.

# DSSA-PPI: Enhancing binding affinity change prediction upon protein mutations using disentangled structure-sequence aware attention

Juhong Wu<sup>1</sup>, Jiehui Sun<sup>1</sup>, Tian Liang<sup>1</sup>, Yongqi Zhang<sup>1</sup>, Han Zhang<sup>1</sup>, Tianyi Zhang<sup>4</sup>, Xianmin Feng<sup>4</sup>, Ping Gao<sup>1</sup>, Peng Xu<sup>2,\*</sup>, Jinyu Li<sup>1,3,5,\*</sup>

<sup>1</sup> College of Chemistry, Fuzhou University, Fuzhou 350116, Fujian, China

<sup>2</sup> College of Biological Science and Engineering, Fuzhou University, Fuzhou 350116, Fujian, China

<sup>3</sup> College of Biological and Pharmaceutical Engineering, Jilin Agricultural Science and Technology University, Jilin 132101, China

<sup>4</sup> Jilin Medical University, Jilin 132013, China

<sup>5</sup> Fujian Provincial Key Laboratory of Theoretical and Computational Chemistry, Xiamen 361005, Fujian, China

## Corresponding authors:

\*Peng Xu, email: [pengxu@fzu.edu.cn](mailto:pengxu@fzu.edu.cn)

\*Jinyu Li, email: [j.li@fzu.edu.cn](mailto:j.li@fzu.edu.cn)



## Abstract

View Article Online  
DOI: 10.1039/D5SC08898D

Accurate assessment of the effects of mutations on protein-protein interactions (PPIs) is crucial for understanding disease pathogenesis and the development of targeted therapies. Here, we present DSSA-PPI, a hybrid deep learning framework that enhances the prediction of mutation-induced binding affinity changes ( $\Delta\Delta G$ ) by leveraging structural and sequence information through a disentangled attention mechanism. Building upon the complementary strengths of a geometric equivariant graph neural network PPIFormer and a protein language model ESM-2, our framework employs a novel representation learning strategy that integrates sequence- and structure-specific contributions, thereby improving the precision of PPI  $\Delta\Delta G$  predictions. DSSA-PPI demonstrates robust performance across diverse mutational contexts on the standard protein binding affinity SKEMPI v2 dataset and outperforms existing methods on multiple benchmarks under identical cross-validation. In a case study of the SARS-CoV-2 receptor-binding motif (RBM) interaction with angiotensin-converting enzyme 2 (ACE2), our model accurately identifies top-ranking mutations that enhance binding affinity. Additionally, it guided the optimization of a peptide inhibitor, improving its inhibitory activity against activated factor XI (FXIa) by over 40-fold. These results highlight DSSA-PPI as a versatile and reliable tool for predicting mutation-induced perturbations in PPIs.

**Keywords:** hybrid deep learning network, protein binding affinity change prediction, protein engineering



## 1. Introduction

Protein-protein interactions (PPIs) govern a wide range of biological processes, including signal transduction<sup>1,2</sup>, immune responses<sup>3,4</sup>, and metabolic regulation<sup>5,6</sup>. Mutations that disrupt or modulate these interactions can lead to dysregulated cellular functions and are implicated in numerous diseases, including cancer<sup>7,8</sup>, autoimmune disorders<sup>9,10</sup>, and neurodegenerative diseases<sup>11,12</sup>. Understanding how amino acid substitutions influence PPIs is critical for elucidating disease mechanisms and developing targeted therapeutic strategies. In protein engineering—particularly in antibody design and binder development—optimizing PPIs often requires exploring vast mutational landscapes, where combinatorial mutations can generate thousands to millions of potential variants. While high-throughput experimental techniques like deep mutational scanning (DMS) enable the large-scale profiling of PPIs<sup>13</sup>, these methods remain resource-intensive and impractical for exhaustively assessing expansive mutational spaces. Consequently, there is an urgent need for accurate and scalable computational approaches to predict the effects of mutations on binding affinity.

Over the years, numerous computational methods have been developed to predict changes in protein-protein binding affinity upon mutations<sup>[11–16]</sup>. Traditional physics-based approaches, such as FoldX<sup>14</sup>, Flex ddG<sup>15</sup>, meta-dynamics<sup>16</sup>, and molecular mechanics/generalized Born surface area (MM/GBSA)<sup>17</sup>, rely on rigorous free-energy calculations but suffer from high computational costs due to extensive conformational sampling requirements. In contrast, machine learning (ML)-based methods offer a more efficient, data-driven alternative. These approaches can be broadly categorized into sequence-based and structure-based models, depending on their input features.

Sequence-based models leverage evolutionary information and physicochemical properties derived from amino acid sequences to infer binding affinity changes. For instance, SAAMBE-SEQ employs hand-crafted sequence features, including position-specific scoring matrices (PSSMs) and physicochemical descriptors, in conjunction with a gradient-boosted tree (GBT) predictor<sup>18</sup>. Similarly, ISLAND integrates sequence-based features with kernel-based similarity measures to enhance prediction accuracy<sup>19</sup>. However,



these methods fail to account for the structural context essential for accurately modeling binding interactions.

Structure-based models, by contrast, utilize geometric representations of protein complexes to encode topological and spatial features, often achieving superior predictive performance. These models can be broadly divided into two categories: featurization-based methods and end-to-end methods. Featurization-based methods rely on hand-crafted or algorithmically derived features to encode the structural and physicochemical properties of protein. A prominent line of work in this category leverages algebraic topology to simplify complex 3D structures while preserving essential biological features, has shown promising potential in the field of mutational effect on protein binding affinity changes prediction. For example, TopNetTree employs element- and site-specific persistent homology to extract topological invariants from protein–protein complexes, effectively capturing their structural complexity for mutation effect prediction<sup>20</sup>. Among the most advanced models in this category, MT-TopLap integrates persistent Laplacian features with physicochemical descriptors and transformer-based protein language model embeddings, achieving superior performance in predicting binding affinity changes<sup>21</sup>. In contrast, end-to-end methods directly learn structural representations from raw input without manual feature engineering. GeoPPI, for example, employs a graph attention network to learn structural representations through a self-supervised side-chain reconstruction task, followed by a GBT predictor to estimate mutational effects<sup>22</sup>. MpbPPI extends this paradigm with an equivariant graph neural network (GNN) and multi-task pre-training to further enhance structure-aware learning<sup>23</sup>. However, both models rely on GBT predictors, which do not explicitly model the physical mechanisms underlying PPI perturbations. Recent advances in geometric deep learning have led to frameworks such as MuToN, which employs a geometric transformer to capture local structural perturbations and receptor-ligand interactions<sup>24</sup>. Despite their promise, these methods remain constrained by their dependence on high-quality structural inputs for mutant complexes. While tools like AlphaFold<sup>25</sup> and RoseTTAFold<sup>26</sup> can predict mutant structures, their computational cost becomes prohibitive when applied to large mutational libraries<sup>27,28</sup>.

View Article Online  
DOI: 10.1039/D5SC08898D



Moreover, selecting the most plausible conformations from multiple predicted structures introduces additional challenges.

To address these limitations, PPIFormer adopts a pre-training strategy inspired by masked language modeling, reconstructing masked structural elements to predict binding affinity changes without requiring explicit mutant structures<sup>29</sup>. By computing the log-odds of probability differences between wild-type and mutant residues, PPIFormer enables predictions based solely on a single input structure. Nevertheless, existing approaches—whether sequence- or structure-based—have yet to fully exploit the complementary strengths of both modalities. For example, ProAffiMuSeq iteratively combines sequence and structural descriptors but lacks a mechanism to model their interdependencies<sup>30</sup>; while ProBASS concatenates embeddings from ESM-2 and ESM-IF1 without explicitly capturing their interplay<sup>31</sup>.

Here, we present DSSA-PPI, a hybrid deep learning framework that integrates sequence and structural information via a cross-attention mechanism to predict mutation-induced changes in protein-protein binding affinity. Building upon PPIFormer, our model retains its advantage of bypassing explicit mutant structures while enhancing predictive accuracy through the incorporation of ESM-2-derived sequence representations. DSSA-PPI demonstrates robust performance across diverse mutational contexts in the SKEMPI v2 dataset and outperforms existing methods on standard benchmarks. Stratified analyses further demonstrate its reliability across mutations of different physicochemical types. We further validate its utility through a case study on SARS-CoV-2 spike protein variants binding to angiotensin-converting enzyme 2 (ACE2), where DSSA-PPI accurately identifies affinity-enhancing mutations and captures key mutational signatures of variants of concern (VOCs). Furthermore, DSSA-PPI successfully guides the engineering of a cyclic peptide inhibitor's binding affinity to activated factor XI (FXIa), validating its practical application. Collectively, these results establish DSSA-PPI as a powerful and versatile tool for predicting mutation-induced perturbations in PPIs.

## 2. Results and Discussion

### 2.1 Overview of DSSA-PPI



The global framework of DSSA-PPI is illustrated in Figure 1A, with detailed architectural components presented in Figure S1. It comprises three primary modules: a structure encoder, a sequence encoder, and a transformer-based fusion block equipped with disentangled attention mechanisms for both structural and sequence information.

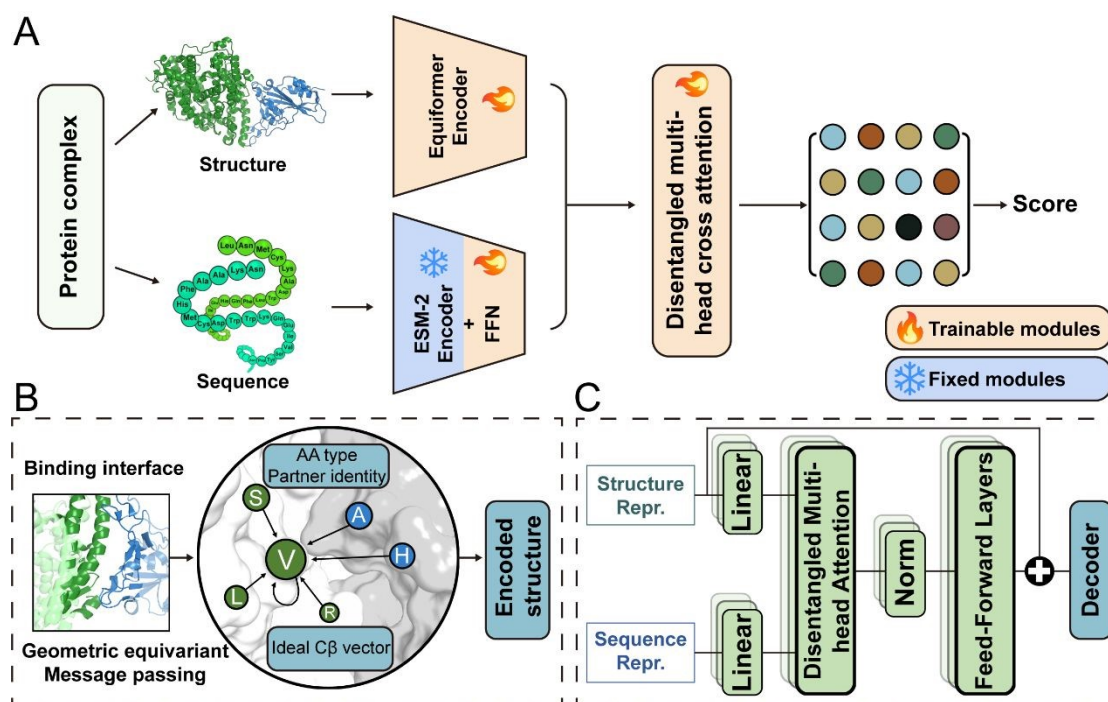


**Figure 1.** An illustrative workflow of DSSA-PPI for predicting mutation effects. (A) For a given protein complex, DSSA-PPI encodes structure and sequence information to generate logits for each residue, which are used to calculate protein binding affinity change upon mutations. (B) The protein complex interface was encoded with a geometric message passing mechanism. (C) The vector representations of structural and sequence information are integrated using a disentangled multi-head cross-attention mechanism.

### 2.1.1 Structure and sequence encoders

The structure encoder adopts the PPIFormer framework. Which encodes protein complex structures using a coarse-grained residue-level graph centered on the binding interface (Figure 1B). Each node represents a residue via its C $\alpha$  atom, with node features categorized into scalar and vectorial states. Scalar features include amino acid identity and binding partner annotations, while vectorial features are derived from geometric calculations using ideal bond angles and lengths. An advanced SE(3)-equivariant graph transformer (Equiformer<sup>32</sup>) encodes these features (Figure S1A), leveraging attention





mechanisms to process both scalar and vectorial data while preserving rotational and translational equivariance. For sequence encoding, we utilize ESM-2, followed by a three-layer feedforward neural network as the predictor. ESM-2 is a state-of-the-art protein language model pre-trained via masked language modeling. It generates contextually rich embeddings that capture evolutionary and functional constraints, enhancing the ability of the model to generalize across diverse protein interactions.

### 2.1.2 Disentangled attention-based fusion module

To effectively integrate structural and sequence information, DSSA-PPI introduces a multi-head disentangled cross-attention mechanism (Figure 1C and Figure S1C). Unlike standard self-attention, this module decomposes attention weights into five components. It captures contributions from structure, sequence, and binding partner sequence to model cross-modality and inter-chain interactions explicitly. The multi-head disentangled attention block fuses structural representations from the SE(3)-equivariant graph transformer with sequence representations derived from ESM-2 (see Methods). By explicitly capturing the interplay between 3D geometry and sequence context, this approach yields a more comprehensive representation of protein complexes, improving predictive accuracy.

### 2.1.3 Pre-training and fine-tuning strategy

To ensure robust learning of PPI structural principles, we pre-trained DSSA-PPI on a large, diverse dataset of 3D protein-protein interfaces using a masked structure modeling (MSM) objective. This task, analogous to masked language modeling in natural language processing, enables the model to infer geometric and sequential features by reconstructing masked structural elements. The pre-trained model thus learns transferable representations of protein interfaces, enhancing its generalization capability. During fine-tuning, we compute the log-odds of logit outputs between wild-type and mutant residues to predict  $\Delta\Delta G$  values. This formulation guarantees antisymmetric predictions (i.e.,  $\Delta\Delta G(\text{wt} \rightarrow \text{mut}) = -\Delta\Delta G(\text{mut} \rightarrow \text{wt})$ ), ensuring thermodynamic consistency in changes to binding affinity.

## 2.2 Performance for protein binding affinity prediction

We conducted a comprehensive evaluation of the predictive performance of DSSA-PPI





using the SKEMPI v2 benchmark dataset, which contains 7,085 experimentally measured mutation effects (including both single and multiple amino acid substitutions) across 345 distinct protein-protein interactions. Following established conventions, we employed a leave-one-complex-out (LOCO) cross-validation and a 10-fold cross-validation strategy, utilizing two distinct splitting methodologies: mutation-level splitting and complex-level splitting. Multiple evaluation metrics were employed to comprehensively evaluate model performance, with Pearson's correlation coefficient (PCC) serving as the primary evaluation criterion.

Under the LOCO split, we limited training to 3 epochs per fold due to the high computational cost of end-to-end training across multiple folds. Despite this constraint, DSSA-PPI maintained competitive performance relative to existing methods (Table S1). For mutation-level splitting, our model achieved an overall PCC of 0.77, a Spearman's correlation of 0.73, and a root-mean-square error (RMSE) of 1.52 for  $\Delta\Delta G$  prediction (Figure 2A). For binary classification of binding affinity changes, the model recorded an area under the receiver operating characteristic curve (AUROC) of 0.85 (Figure 2B). Notably, the model exhibited consistent performance across folds in mutation-level cross-validation. In contrast, larger variability was observed in complex-level evaluation, suggesting that mutation-level splitting may overestimate performance due to potential information leakage among mutations within the same complex (Table S2).

We further evaluated the predictive performance of DSSA-PPI across varying mutational distances. While the model demonstrated consistent and robust performance on mutation-level splitting, its performance declined on the more challenging complex-level splitting, which involves testing on unseen protein complex structures (Figure 2C). Specifically, the model exhibited reduced accuracy at higher mutational distances (mutational distance > 3). Such cases often involve extensive or highly disruptive alterations that may induce complex changes in protein-protein interactions, including significant conformational rearrangements. These dynamic structural perturbations present a fundamental challenge, as the current model implicitly assumes moderate local shifts upon mutation and does not explicitly model large-scale conformational changes. The impact of protein dynamics is a well-recognized limitation in this field<sup>33–35</sup>. Future



extensions incorporating global dynamic features, such as those captured by the Gaussian Network Model (GNM)<sup>38</sup> and the Anisotropic Network Model (ANM)<sup>36</sup>, may help improve predictive performance in these challenging scenarios. With the rapid advancement of deep learning frameworks capable of modeling protein conformational ensembles<sup>37–39</sup>, fully integrating dynamic information into  $\Delta\Delta G$  prediction is expected to become increasingly feasible.

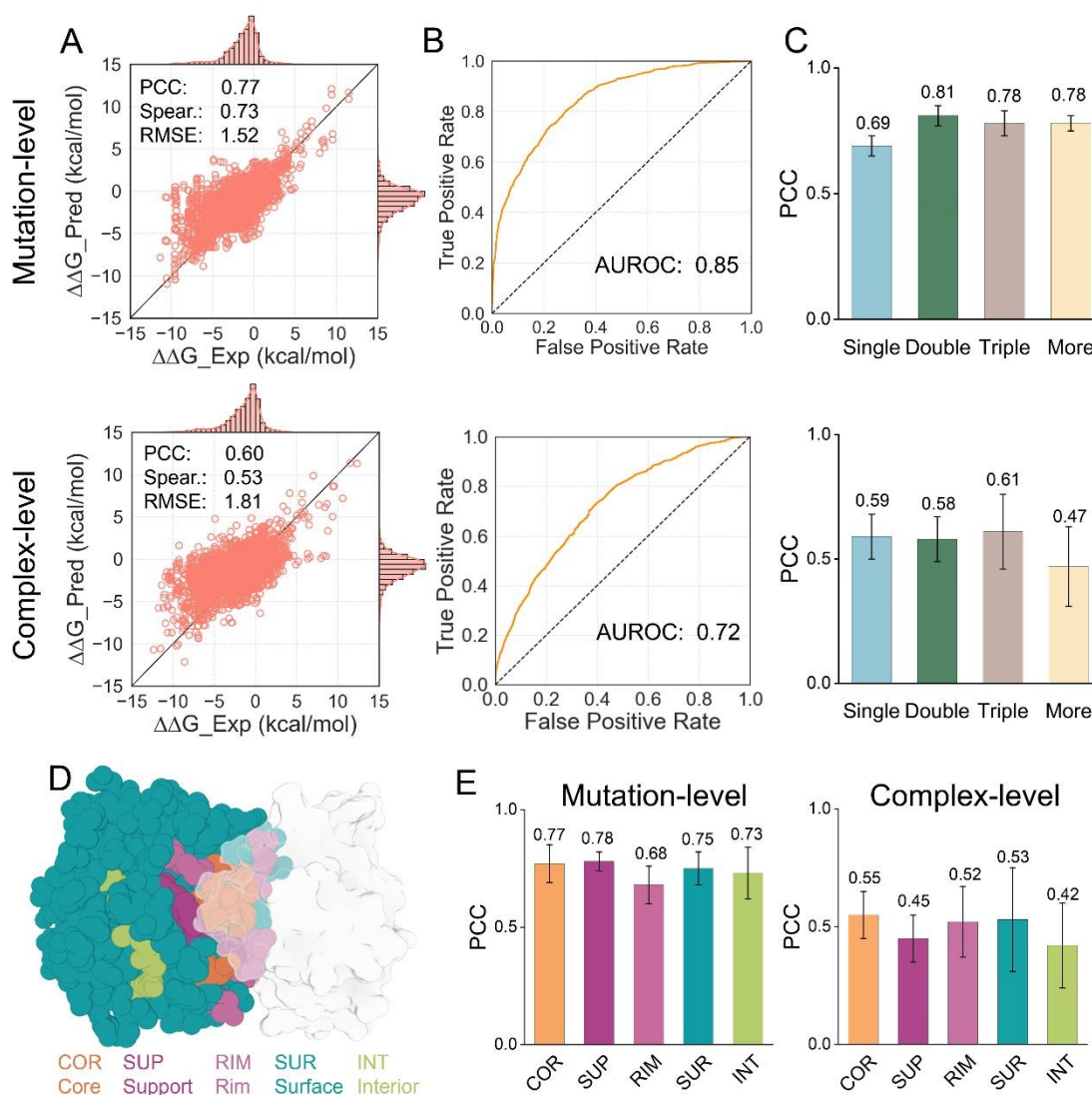


**Figure 2.** DSSA-PPI predicts binding affinity changes of PPIs upon mutations. (A-C, E) Two distinct dataset splitting strategies were employed to evaluate the performance of DSSA-PPI: mutation-level splitting and complex-level splitting. (A) Regression plots comparing predicted and experimental binding affinity changes ( $\Delta\Delta G$ ) for all mutations in the SKEMPI v2.0 dataset. (B) AUROC for binary classification of binding affinity changes, distinguishing between increases and decreases in SKEMPI v2.0. (C) Prediction performance across different mutation distances, with Pearson correlation coefficient (PCC)



and standard deviations reported from tenfold cross-validation. (D) A schematic illustration of the structural regions of proteins, highlighting core (COR), support (SUP), rim (RIM), surface (SUR), and interior (INT) regions. (E) Prediction results across different mutation locations, with PCC and standard deviations obtained from tenfold cross-validation for both splitting strategies.

Finally, we investigated the predictive ability of DSSA-PPI across different structural regions of protein complexes. Using the SKEMPI v2 annotations, the dataset was categorized into core (COR), support (SUP), rim (RIM), surface (SUR), and interior (INT) regions based on mutation locations (Figure 2D). Notably, despite being trained exclusively on binding interface residues, DSSA-PPI maintained consistent predictive accuracy across all structural areas (Figure 2E).

### 2.3 Ablation analysis of model components

To elucidate the contributions of key components in our model architecture, we conducted a series of ablation experiments. Specifically, we examined the effects of (i) removing the sequence encoder and (ii) replacing the disentangled attention fusion module with a simple concatenation operation. As presented in Table 1, both modifications resulted in notable performance degradation, underscoring the importance of these components. These results indicate that: (i) evolutionary context captured by the sequence encoder is essential for accurate prediction of binding affinity changes, and (ii) the disentangled attention mechanism facilitates a more effective integration of structural and sequence-based features than naïve concatenation.

To further assess the contributions of individual attention terms in the disentangled attention module, we performed ablations by removing one term at a time: including structure-to-structure (R2R), structure-to-sequence (R2S), structure-to-partner sequence (R2S<sub>partner</sub>), sequence-to-structure (S2R), partner sequence-to-structure (S<sub>partner</sub>2R). These ablation results reveal that all five terms are necessary to achieve the best overall performance. Notably, the removal of R2R and R2S results in drops in overall performance, with the PCC decreasing from 0.77 to 0.75 and 0.76, respectively. This underscored the important role of structure information and structural representation to attend to its own



sequence context. Removing of  $S_{\text{partner}2R}$  have least impact, suggesting that binding partner sequence attention to structure is relatively less critical than other items.

Collectively, these findings validate our architectural design and emphasize the critical role of synergistically combining structural and sequence information, as well as the necessity of each individual attention term, for robust and accurate prediction of binding affinity changes.

**Table 1.** Ablation experiment on key components of DSSA-PPI and different disentangled terms. Results are reported on mutation-level split of the SKEMPI v2.0 dataset.

	PCC $\uparrow$	Spearman $\uparrow$	RMSE $\downarrow$	AUROC $\uparrow$
DSSA-PPI	0.77	0.73	1.52	0.85
– w/o seq. enc.	0.74	0.68	1.72	0.80
– w/o cross-attn.	0.72	0.65	1.80	0.77
– w/o R2R <sup>a</sup>	0.75	0.70	1.65	0.80
– w/o R2S	0.76	0.71	1.59	0.83
– w/o R2S <sub>partner</sub>	0.77	0.71	1.54	0.84
– w/o S2R	0.76	0.71	1.53	0.83
– w/o $S_{\text{partner}2R}$	0.76	0.70	1.53	0.85

<sup>a</sup> The term "– w/o R2R" denotes the removal of structure-to-structure attention term, similar to other terms.

## 2.4 Benchmarking against existing methods under identical complex-level cross-validation

To establish the predictive capabilities of DSSA-PPI, we conducted comprehensive benchmarking against the very recent approaches using three widely adopted datasets: S1131, S4169, and M1707. As a baseline comparison, we first performed random 10-fold mutation-level cross-validation. As shown in Table S3, all machine learning-based methods, including DSSA-PPI, exhibited strong performance across benchmarks under this setting.

However, recent studies have raised significant concerns that random mutation-level splits can lead to overly optimistic performance estimates<sup>40,41</sup>, particularly when mutations from



the same protein complex appear in both training and test sets. Consistent with these observations, we also found that performance metrics under mutation-level splitting were substantially higher than those obtained under complex-level cross-validation (Figure 2A–B and Table S2).

To address this, we adopted a more rigorous evaluation protocol based on complex-level splitting, following the protocol of MpbPPI, which ensures that mutations from the same protein complex do not appear across different folds. We adopted predefined five-fold complex-level cross-validation splits for S1131 and S4169 from MpbPPI. For M1707, which lacks predefined partitions, we created analogous complex-level splits based on PDB identifiers to ensure methodological consistency. To ensure robust performance estimation, we repeated five-fold cross-validation five times using independent random seeds for each dataset. The same data splits were applied consistently across all baseline methods to ensure fair comparisons.

Across all benchmarks, DSSA-PPI generally outperformed baseline models on both regression (PCC, RMSE) and classification (AUROC) tasks (Table 2 and Table S4). On the S1131 dataset, which consists of non-redundant single-point mutations localized at protein–protein interfaces, DSSA-PPI achieved a PCC of 0.71 and an AUROC of 0.77. This performance exceeded that of PPIFormer (PCC: 0.68, AUROC: 0.72), MT-TopLap (PCC: 0.62, AUROC: 0.72), ESM-2 with a three-layer feedforward network regressor (ESM-2-FFN) (PCC: 0.65, AUROC: 0.74), ProBASS (PCC: 0.65, AUROC: 0.80), and SAAMBE-SEQ (PCC: 0.49, AUROC: 0.70). On the S4169 dataset, which includes a more diverse mutation landscape, DSSA-PPI maintained strong performance with a PCC of 0.58 and AUROC of 0.70. For the challenging M1707 dataset—characterized by up to nine mutations across multiple chains within a single complex—DSSA-PPI achieved a PCC of 0.42 and AUROC of 0.72.

Compared with physics-based approaches, DSSA-PPI also showed superior performance across S1131, S4169, and M1707 (Table S5). Under current benchmarking protocols, structure-based methods, including physics-based tools, are typically evaluated on single static structures because generating conformational ensembles through molecular dynamics is computationally demanding. This practice does not reflect the full



capabilities of physics-based methods, which generally achieve higher accuracy when conformational sampling is incorporated<sup>17,42</sup>. In contrast, ML-based models have been shown to exhibit greater robustness to structural variability, as reported in several studies<sup>23,24</sup>. A systematic benchmarking framework that evaluates both physics-based and machine learning based methods using dynamically sampled conformations would provide a more balanced and rigorous comparison. Although such an assessment is beyond the scope of the present study, it represents an important direction for future work.

**Table 2.** Comparison of model performance on the benchmark datasets S1131, S4169 and M1707 under identical 5-fold complex-level cross-validation.<sup>a</sup> Data are represented as mean  $\pm$  SD (n=5).

Method	S1131		S4169		M1707	
	PCC $\uparrow$	AUROC $\uparrow$	PCC $\uparrow$	AUROC $\uparrow$	PCC $\uparrow$	AUROC $\uparrow$
DSSA-PPI	<b>0.71 <math>\pm</math> 0.01</b>	0.77 $\pm$ 0.02	<b>0.58 <math>\pm</math> 0.01</b>	<b>0.70 <math>\pm</math> 0.02</b>	<b>0.42 <math>\pm</math> 0.02</b>	<b>0.72 <math>\pm</math> 0.02</b>
PPIFormer	0.68 $\pm$ 0.01*	0.72 $\pm$ 0.02*	0.54 $\pm$ 0.01*	0.60 $\pm$ 0.01*	0.31 $\pm$ 0.03*	0.61 $\pm$ 0.02*
ESM-2-FFN <sup>b</sup>	0.65 $\pm$ 0.02*	0.72 $\pm$ 0.02*	0.45 $\pm$ 0.02*	0.62 $\pm$ 0.02*	0.25 $\pm$ 0.05	0.63 $\pm$ 0.02*
MT-TopLap	0.62 $\pm$ 0.03*	0.74 $\pm$ 0.01*	0.50 $\pm$ 0.03*	0.64 $\pm$ 0.01*	—	—
MuToN	0.70 $\pm$ 0.01	0.74 $\pm$ 0.01	0.57 $\pm$ 0.01	0.64 $\pm$ 0.01*	—	—
MpbPPI	0.48 $\pm$ 0.04*	0.75 $\pm$ 0.02*	0.43 $\pm$ 0.03*	0.67 $\pm$ 0.01*	0.34 $\pm$ 0.02*	0.64 $\pm$ 0.02*
ProBASS	0.65 $\pm$ 0.01*	<b>0.80 <math>\pm</math> 0.01</b>	0.51 $\pm$ 0.01*	0.68 $\pm$ 0.03	0.20 $\pm$ 0.04*	0.59 $\pm$ 0.02*
SAAMBE-SEQ	0.49 $\pm$ 0.01*	0.70 $\pm$ 0.02*	0.29 $\pm$ 0.01*	0.59 $\pm$ 0.01*	—	—
FoldX	0.44	0.70	0.30	0.62	0.30	0.59

<sup>a</sup> Bold values indicate the best results. The dash sign indicates the results of the corresponding methods are not available.

<sup>b</sup> ESM-2-FFN refers to the ESM-2 model followed by a three-layer feed-forward network, which shares the same architecture as the sequence encoder used in DSSA-PPI.

\* Indicates statistically significant difference compared to DSSA-PPI ( $p < 0.05$ ), determined by a one-tailed unpaired t-test.

Beyond numerical performance, we conducted an in-depth architectural analysis to elucidate the sources of the predictive advantage of DSSA-PPI. We benchmarked it against five representative ML-based baseline models: PPIFormer (structure-based), ESM-2-FFN (sequence-based), ProBASS (structure–sequence hybrid), MT-TopLap (topology-based hybrid), and SAAMBE-SEQ (biophysics-informed), as summarized in





Table S6.

View Article Online  
DOI: 10.1039/D5SC08898D

Our comparative analysis revealed several key insights. First, end-to-end deep learning models generally outperformed methods based on handcrafted features, such as SAAMBE-SEQ, across all datasets. Interestingly, PPIFormer outperformed ESM-2-FFN in regression tasks, while ESM-2-FFN generally showed superior performance in classification (Table 2). This divergence may suggest that structural and sequence representations encode distinct but complementary aspects of protein binding. ProBASS attempts to leverage this by fusing multimodal embeddings from ESM-IF and ESM-2 via simple feature concatenation. While this yielded modest improvements over ESM-2-FFN on S4169 datasets (PCC of 0.51 vs. 0.45), it failed to generalize well to more complex cases such as M1707, where performance decreased compared to the ESM-2 backbone (PCC: 0.20 for ProBASS vs. 0.25 for ESM-2-FFN). A similar pattern was observed with MT-TopLap, which combines ESM-2 embeddings with handcrafted topological features. Despite this multimodal feature fusion, MT-TopLap did not outperform ESM-2-FFN, indicating that naive feature concatenation may not be sufficient to capture the complex interplay between structure and sequence representations.

By contrast, DSSA-PPI builds upon PPIFormer and ESM-2, but employs a disentangled structure–sequence attention module specifically designed to model inter-modal interactions. This architecture consistently outperforms both backbone models across benchmark datasets. To further assess the generality of the disentangled attention design, we evaluated DSSA-PPI-PF, a variant where the structure encoder is initialized with PPIFormer pre-trained weights and the pretraining is omitted. Despite lacking co-adaptive structure–sequence pretraining, DSSA-PPI-PF still outperformed PPIFormer and achieved performance comparable to the fully end-to-end DSSA-PPI model (Table S7). This finding highlights the plug-and-play robustness and effectiveness of the disentangled attention module.

In summary, our architectural investigation indicates that the performance gains of DSSA-PPI stem from the disentangled attention mechanism, which facilitates synergistic integration of structural and sequential representations.





## 2.5 Stratified performance analysis based on chemical characteristics mutation types

Having established the overall predictive superiority of DSSA-PPI on benchmark datasets, we next sought to examine its predictive performance in a more fine-grained manner. To this end, we conducted a systematic error analysis stratified by amino acid chemical properties. This analysis leveraged the S4169 dataset, which comprises all single-point mutations from the SKEMPI v2.0 database. Predictive performance was assessed using PCC and AUROC, averaged over five repetitions of five-fold cross-validation.

We first categorized mutations based on the chemical characteristics of the substituted residues: charged, polar, hydrophobic, and special cases (Gly, Cys, Pro). As shown in Figure 3A-B, DSSA-PPI demonstrated consistent performance across most categories. For regression, all groups achieved a PCC greater than 0.4, with four categories exceeding 0.8. In the classification setting, DSSA-PPI also performed reliably, with AUROC scores above 0.6 across all categories. These results suggest that DSSA-PPI captures the general physicochemical behavior of amino acid substitutions, enabling generalization across diverse mutation types. Due to the severe class imbalance in the S4169 dataset, we did not perform further breakdown analysis at the level of individual wild-type to mutant amino acid pairs (Figure S2).

To further investigate specific failure modes, we manually inspected the top 10 mutations with the largest absolute prediction errors ( $|\Delta\Delta G_{\text{Exp}} - \Delta\Delta G_{\text{Pred}}|$ ). These outlier mutations often involved wild-type residues participating in intricate multichain interactions or exhibiting extreme physicochemical shifts. For instance, in PDB complex 2NZ9 (Figure 3C), the wild-type H10641<sup>A</sup> participates in hydrogen bonding with D102<sup>D</sup> and G95<sup>C</sup>, and engages in  $\pi$ - $\pi$  stacking with F36<sup>C</sup>. Upon mutation to alanine, DSSA-PPI correctly predicted a decrease in binding affinity but substantially underestimated the magnitude of  $\Delta\Delta G$ , likely due to the disruption of multichain cooperative interactions that are difficult to model and may not be fully captured by the coarse-grained, residue-level representations employed in DSSA-PPI. Another failure case involves a drastic substitution from tryptophan to arginine in 1MAH. The wild-type tryptophan resides in a tightly packed hydrophobic pocket at the interface (Figure 3D). Introducing a charged arginine residue



alters the local electrostatic environment and induces desolvation penalties. DSSA-PPI

[View Article Online](#)  
[DOI: 10.1039/D5SC08898D](#)

failed to fully capture this physicochemical disruption, underestimating the binding destabilization.

These findings suggest that while DSSA-PPI demonstrates strong overall performance, it faces challenges in specific edge cases involving complex interaction networks. In such cases, the perturbations introduced by certain substitutions may not be fully captured by the coarse-grained, residue-level representations used in DSSA-PPI. Future improvements could include incorporating explicit side-chain modeling or surface-based physicochemical representations to better characterize the local interaction environment and enhance prediction accuracy in structurally intricate contexts.



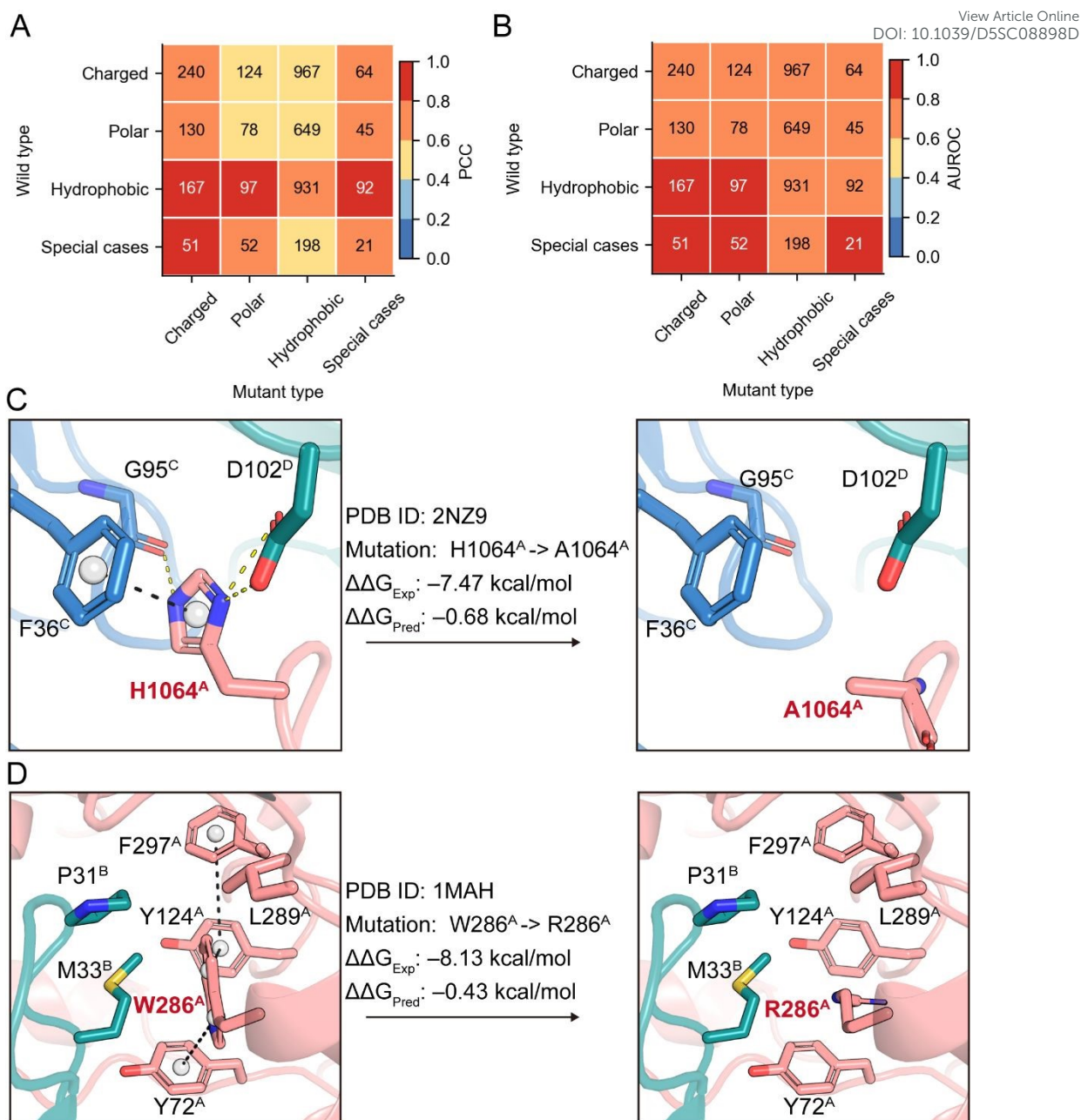


**Figure 3.** Stratified performance analysis and case studies on mutation prediction. (A) PCC and (B) AUROC scores for DSSA-PPI predictions, stratified by the chemical class of wild-type and mutant amino acids: charged, polar, hydrophobic, and special cases. Each cell indicates the number of mutation samples in the corresponding category. (C–D) Representative failure cases with significant absolute prediction errors. Involving (C) a complex multichain interaction network and (D) extreme physicochemical shifts. Hydrogen bonds and  $\pi$ - $\pi$  stacking interactions are depicted as yellow and black dashed lines, respectively.

## 2.6 Evaluation on SARS-CoV-2 RBM mutations affecting ACE2 binding

To further demonstrate the predictive power of our model, we evaluated its performance on the fitness of binding affinity changes induced by mutations in the receptor binding motif



(RBM) of the receptor binding domain (RBD) of the SARS-CoV-2 spike protein, which directly interacts with the human ACE2 receptor (Figure 4A). We employed an ensemble model trained via 10-fold cross-validation on SKEMPI v2, with predictions averaged for robustness. All comparative models were evaluated under identical conditions to ensure fair benchmarking. As the MT-TopLap was pretrained directly on the SARS-CoV-2 RBD/ACE2 deep mutational scanning (DMS) dataset<sup>21,43</sup>, it was excluded from this case study to maintain an unbiased comparison.

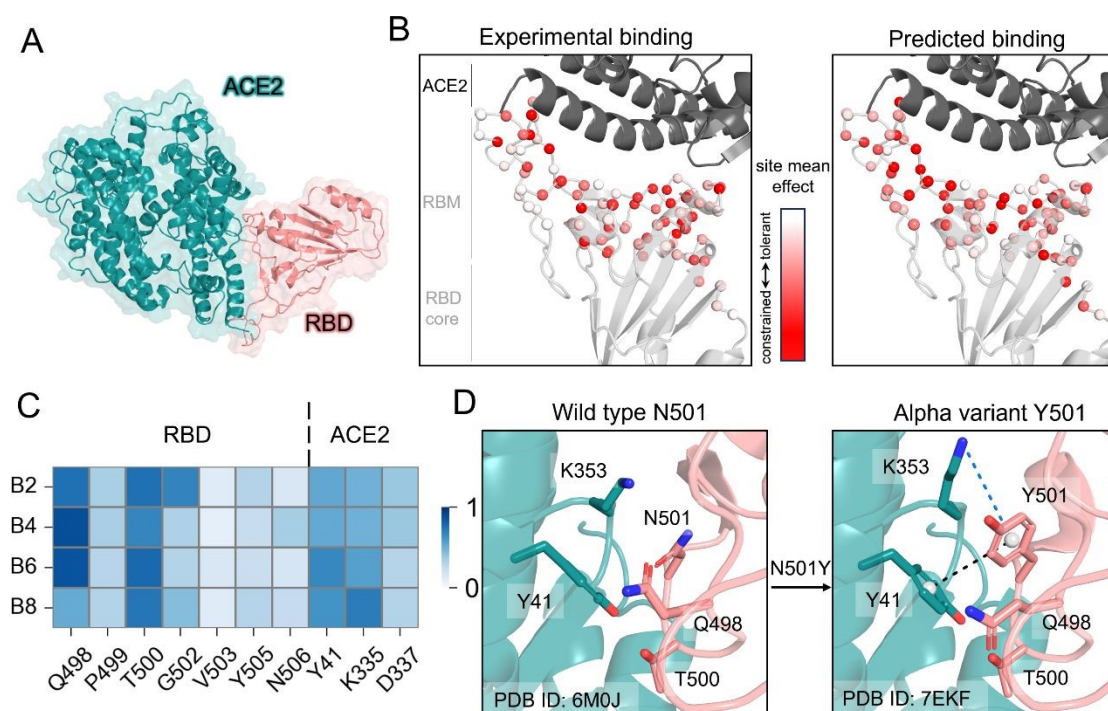


**Figure 4.** Case study involving the evaluation of SARS-CoV-2 RBM interacting with ACE2. (A) Crystal structure of RBD/ACE2 complex (PDB ID: 6M0J). (B) Comparative analysis of experimental and DSSA-PPI predicted mutational constraints of ACE2-binding mapped onto the SARS-CoV-2 RBD structure. (C) Attention heatmap from blocks 2, 4, 6, and 8 of DSSA-PPI, centered on residue N501. The map highlights strong intra-chain attention to Q498 and T500, as well as prominent inter-chain attention to Y41 and K353 on ACE2. (D) Structural comparison of wild-type (N501) and Alpha variant (Y501) interactions at the RBD-ACE2 interface. Cation- $\pi$  and  $\pi$ - $\pi$  stacking interactions are depicted as blue and black dashed lines, respectively.

We conducted saturation single-point mutational analysis on approximately 1,700 RBM mutations, with predictions completed within seconds for DSSA-PPI, demonstrating high computational efficiency. Compared to DMS experimental data<sup>44</sup>, DSSA-PPI



consistently outperformed all baseline methods across multiple evaluation metrics (Table 3 and Table S8). Notably, DSSA-PPI predictions captured the overall mutational impact patterns observed in DMS data at both the site level (Figure 4B) and the mutation level (Figure S3). Additionally, we employed a hit-rate metric to assess the ability of models to prioritize top-ranking mutations. Among the top 10 high-affinity mutations identified by DMS experiments, DSSA-PPI successfully identified 4 within the top 1% (18 mutations) and 6 within the top 5% (86 mutations) of its predictions. In comparison, PPIFormer, ESM-2-FFN, and MuToN identified 2, 2, and 1 mutation(s) within the top 5%, respectively. MpbPPI, ProBASS, SAAMBE-SEQ, and FoldX failed to rank any of these mutations within the thresholds.

**Table 3.** Performance comparison of DSSA-PPI and baseline methods on RBM of SARS-CoV-2 interacting with ACE2.

Method	Spearman $\uparrow$	Top10Hit@1% $\uparrow$	Top10Hit@5% $\uparrow$
DSSA-PPI	0.31	40%	60%
PPIFormer	0.19	0%	20%
ESM-2-FFN	-0.04	0%	20%
MuToN	-0.01	0%	10%
MpbPPI	0.08	0%	0%
ProBASS	-0.01	0%	0%
SAAMBE-SEQ	-0.20	0%	0%
FoldX	-0.65	0%	0%

Further, we investigated hot-spot mutations in the RBM region that are associated with early SARS-CoV-2 variants of concern (VOCs), including N501Y, E484K, T478K, K417N, L452R, and Q493R. We compared the ranking and predicted binding fitness scores from DSSA-PPI with experimental data from DMS relative to the wild-type spike protein (Table 4). In general, DSSA-PPI ranked these hot-spot mutations in a manner consistent with experimental data, except for E484K. Interestingly, while DMS reported T478K and Q493R as mildly destabilizing mutations, DSSA-PPI predicted both to be stabilizing, aligning with their known roles in enhancing ACE2 binding in the Delta and Omicron variants<sup>45,46</sup>. These discrepancies suggest that DSSA-PPI may capture co-evolutionary and contextual





information beyond the wild-type sequence, potentially enabling the identification of future adaptive mutations. Additionally, DSSA-PPI ranked N501Y as a top affinity-enhancing mutation, consistent with its well-established role in strengthening ACE2 binding. To probe the model's underlying reasoning, we visualized the attention scores associated with residue N501. The attention map revealed that N501 predominantly attends to Q498 and T500 within the RBD, as well as Y42 and K353 on ACE2 (Figure 4C). Notably, the inter-chain attention patterns align with structural evidence: N501Y forms a  $\pi$ - $\pi$  stacking interaction with Y42 and a cation- $\pi$  interaction with K353 (Figure 4D), both of which are known to enhance ACE2 binding. These results underscore the efficiency and predictive accuracy of DSSA-PPI, and suggest its ability to identify mutations of high biological relevance.

**Table 4.** Comparison of experimental and DSSA-PPI-predicted rankings and fitness scores for key RBM mutations in SARS-CoV-2 VOCs.

Mutation	N501Y	E484K	T478K	K417N	L452R	Q493R
Exp. Rank (%) <sup>a</sup>	0.24%	4.88%	22.03%	52.23%	4.11%	29.61%
Pred. Rank (%)	0.06%	70.56%	13.69%	52.35%	12.93%	2.29%
Exp. Score	1.07	0.09	-0.13	-0.89	0.13	-0.28
Pred. Score	1.85	-1.24	0.13	-0.72	0.16	0.74

<sup>a</sup> Experimental rankings (%) represent the percentile of each mutation's binding fitness relative to all ~1700 single-point RBM mutations in the DMS dataset. A lower percentile indicates higher binding affinity.

## 2.7 DSSA-PPI-guided reengineering of a peptide inhibitor against activated factor XI (FXIa)

Given the superior performance of DSSA-PPI in predicting and ranking mutation-induced changes in binding affinity, we next sought to assess its applicability in the design of peptide inhibitors of serine proteases. As a model system, we re-engineered a cyclic peptide inhibitor of murine urokinase-type plasminogen activator (muPA), mupain-1 (CPAYSRYLDC), to improve its affinity toward FXIa (Figure 5A), an emerging target for low-hemorrhagic antithrombotic therapy<sup>47,48</sup>. Mupain-1 was originally identified through phage display as a selective inhibitor of muPA<sup>49</sup>, but has negligible inhibitory activity against FXIa ( $K_i > 1000 \mu\text{M}$ )<sup>50</sup>, making it an ideal starting point for DSSA-PPI-guided optimization.



To adapt DSSA-PPI for peptide–protease interactions, we fine-tuned the model on the SKEMPI v2.0 dataset, which comprises experimentally validated protein–peptide interaction data. Binding affinity measurements of mupain-1 variants targeting plasma kallikrein (PK)<sup>50</sup>—a serine protease homologous to FXIa—were used as an independent validation set to select the refined model exhibiting the highest Spearman correlation. The optimized DSSA-PPI was subsequently employed to predict and prioritize mutations that could enhance mupain-1 binding to FXIa.

A systematic single-point mutation scan revealed that hydrophobic substitutions at D9 were most likely to improve FXIa affinity (Figure S4). However, given the intrinsically weak binding of the parental peptide ( $K_i > 1000 \mu\text{M}$ ), we reasoned that single-site substitutions might not achieve sufficient enhancement. We therefore performed an exhaustive two-site combinatorial mutation scan, in which all possible double mutants were generated and ranked according to their predicted  $\Delta\Delta G$  values. Analysis of the top 50 predicted variants (Figure 5B) revealed that the cyclic architecture was strictly conserved, with cysteine residues at positions 1 and 10 retained, consistent with their established critical role in maintaining peptide binding affinity<sup>49</sup>. Hydrophobic substitutions at D9 were strongly favored, consistent with the single-point scan, while substitutions of Y7 with alanine occurred at relatively high frequency. Guided by these predictions, two candidate peptides were designed: CPAYSRALFC (FXI-1) and CPAYSRALWC (FXI-2). To further enhance FXIa binding, the arginine residue at position 6 was replaced with a non-natural analogue (L-3-(N-amidino-4-piperidyl)alanine), previously shown to non-specifically improve affinity towards multiple serine proteases<sup>50,51</sup>. Experimental validation confirmed that both designed peptides exhibited markedly enhanced FXIa binding affinity, with  $K_i$  values of  $117 \pm 4 \text{ nM}$  for FXI-1-16 and  $63.5 \pm 2.2 \text{ nM}$  for FXI-2-16 (Figure 5C and S5), compared with  $2560 \pm 350 \text{ nM}$  for the parental mupain-1-16<sup>50</sup>. These engineered peptides therefore provide promising starting points for further optimization toward potent FXIa inhibitors for anticoagulant development.





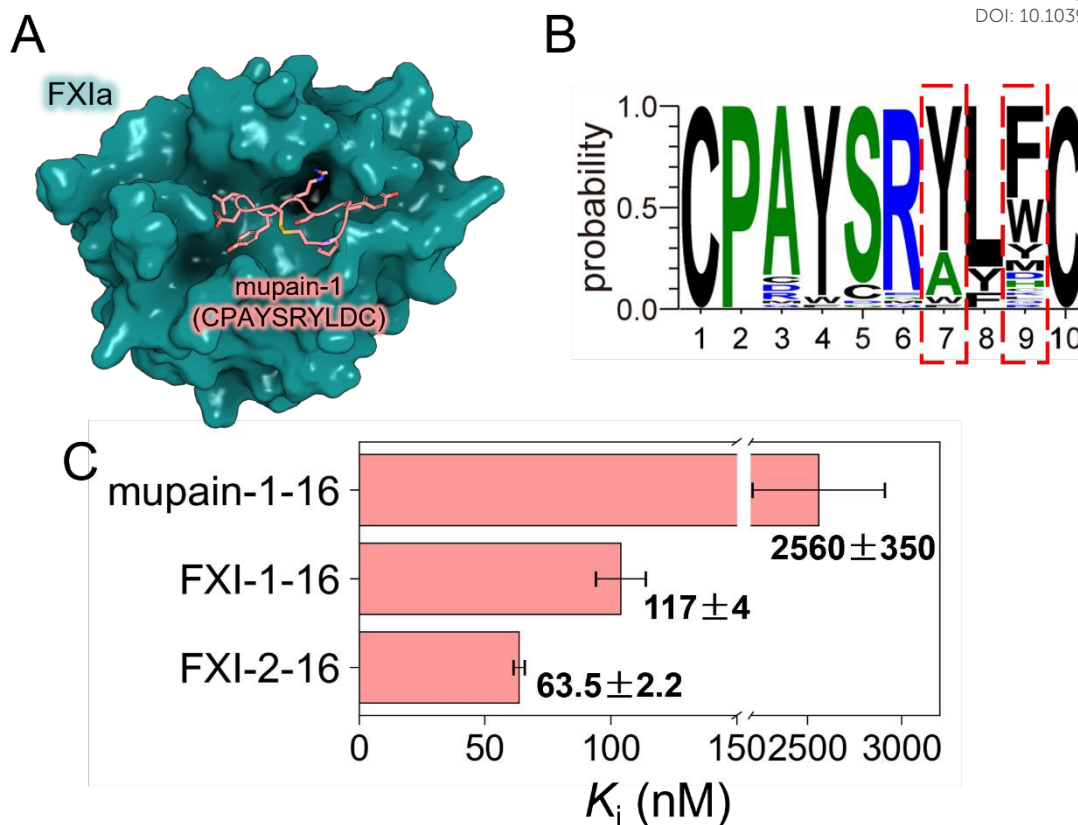


**Figure 5.** Reengineering of mupain-1 against FXIa guided by DSSA-PPI. (A) Structural model of the FXIa–mupain-1 complex. (B) Preferred amino acid frequencies at each position among the top 50 DSSA-PPI–predicted variants, highlighting mutation hotspots at Y7 and D9. (C) Binding affinities ( $K_i$ , nM) of the peptides toward human FXIa are shown as mean  $\pm$  SD ( $n = 3$ ). Data for mupain-1-16 are from Xu et al.<sup>50</sup>

Collectively, these results demonstrate the practical utility and transferability of DSSA-PPI in guiding peptide optimization and protein engineering, enabling rapid identification of high-affinity variants.

### 3. Conclusions

In this study, we introduced DSSA-PPI, a deep learning framework for predicting changes in protein-protein binding affinity induced by amino acid mutations. DSSA-PPI overcomes the limitations of structure-based models, which require precise mutant structures, by achieving superior or competitive performance using only a single wild-type structure. Through the synergistic integration of structural and sequence information, our model demonstrated strong predictive accuracy across diverse benchmark datasets and



outperformed existing approaches in affinity prediction. Stratified analyses further demonstrated its reliability across mutations of different physicochemical types. The practical utility of DSSA-PPI was shown in two case studies. First, the model accurately identified high-affinity mutations in the SARS-CoV-2 RBM interacting with ACE2. Second, it successfully guided the reengineering of a peptide inhibitor targeting FXIa. These results highlight its potential for real-world protein engineering applications. However, like other current approaches, DSSA-PPI exhibits reduced predictive accuracy for highly disruptive mutations (i.e., mutational distance > 3) that may induce large-scale conformational changes. This limitation underscores the need for future work to incorporate structural dynamics for improved prediction. In summary, DSSA-PPI provides an efficient tool for protein-protein interaction engineering, offering valuable insights for rational protein design and therapeutic development.

## 4. METHODS

**Overview of DSSA-PPI architecture.** DSSA-PPI is composed of three main components: (i) structure encoder, (ii) sequence encoder, and (iii) disentangled attention-based fusion module. The framework is initially pre-trained on the PPIRef50K dataset, followed by fine-tuning for downstream protein-protein binding affinity prediction to evaluate its performance.

**Constructing attributed graph for interface.** We first used PDBFixer v1.8 for each protein-protein complex to model the residue geometry coordinates if they are missing in PDB structures. Then, we represented the protein complexes as an attributed graph for their interface at the residue level. Interface residues are identified based on the Euclidean distance between their heavy atoms. A residue is considered part of the interface if the distance to the nearest residue from the binding partner is within a specific distance cutoff (10 Å for the pre-training dataset and 15 Å for SKEMPI v2 datasets). The attributed graph was defined as  $G = (V, E)$ , where  $V$  is the set of residues in the protein complex interface (each residue node is represented by its C $\alpha$  atom) and  $E$  is the set of edges between them. For each residue node  $v_i \in V_{i=1}^N$ , where  $N$  is the number of residues, its feature is



represented as  $v_i = \{x_i, F_i^0, F_i^1\}$ ,  $x_i \in \mathbb{R}^3$  is the C $\alpha$  coordinate of the  $i$ th residue.  $F_i^0, F_i^1$  are two kinds of feature: type-0 scalars (3D-invariant)  $F_i^0 \in \mathbb{R}^{21}$ , and type-1 vectors (3D-equivariant)  $F_i^1 \in \mathbb{R}^{1 \times 3}$ . Feature  $F_i^0$  contains the one-hot encoded representations of the interface residue type (dimension of 20) and a semantic binary value indicating its location in a binding partner. Feature  $F_i^1$  represents virtual beta-carbon orientations, calculated using backbone atom positions (C $\alpha$ , N, C atoms) based on ideal bond angles and lengths<sup>52</sup>. To capture the interactive relationships between residues, we define E as a  $\{0, 1\}^{N \times N}$  matrix, where 1 indicates an edge between two residue nodes if the Euclidean distance between them is less than 7 Å; otherwise, it is 0.

**Geometric structure encoder.** Geometric properties like translational invariance and rotational equivariance are essential in protein-related representation learning. To incorporate these inductive biases, we build our structure encoder on Equiformer<sup>32</sup>, a transformer-based SE(3)-equivariant graph attention network. Equiformer enables the model to learn geometric representations that are equivariant to 3D rotations and translations by operating on features expressed as irreducible representations of the SE(3) group. These features can correspond to different rotation orders: type-0 (scalars), type-1 (vectors), and higher-order tensors.

In our framework, following the design of PPIFormer<sup>29</sup>, we construct our geometric structure encoder using eight stacked SE(3)-Equiformer blocks (Figure S1A). Each block performs message passing over the protein interface graph and updates type-specific features via an attention mechanism that respects SE(3) symmetry. The input to each block  $l$  is the graph  $G$ , with node coordinates  $X \in \mathbb{R}^{N \times 3}$  and connection matrix  $E$ , along with node feature matrices  $H_k \in \mathbb{R}^{N \times d_k \times (2k+1)}$  of different types  $k \in \{0, 1\}$ . The layer-wise update process is defined as follows:

$$h_0^{(1)}, h_1^{(1)} = f(G(X, E, F_0, F_1)) \quad (1)$$

$$h_0^{(l)}, h_1^{(l)} = f(G(X, E, H_0^{(l-1)}, H_1^{(l-1)})), l = 2, \dots, 8 \quad (2)$$

where  $f$  denotes a single SE(3)-Equiformer block. After eight layers of updates, the final type-0 (scalar) output representation  $h_0^{(8)}$  is extracted as the structural representations. The output dimensionality of the encoded structural features is set to 128.



**Sequence encoder.** To model the sequence-level information of protein–protein complexes, we employ ESM-2, a state-of-the-art pretrained protein language model. ESM-2 is trained on over 250 million protein sequences using a masked language modeling (MLM) objective, enabling it to capture rich contextual and evolutionary signals directly from sequence data. For each protein–protein complex. We extract the amino acid sequences of both binding partners. These sequences are either retrieved from the PDB database using the complex's PDB code or directly parsed from the input PDB structure file. Each sequence of the protein complex is then encoded into a 1280-dimensional vector, obtained from the 33th layer embedding of ESM-2. These sequence embeddings are then processed by a parameter-shared feed-forward network (FFN) comprising three hidden layers, each with a hidden dimension of 256. The FFN maps the 1280-dimensional input down to a 128-dimensional output vector (Figure S1B). These embeddings are subsequently fused with the structural representations derived from the geometric encoder for downstream binding affinity change prediction.

**Disentangled attention-based fusion module.** To fully exploit a given protein complex's structural and sequence information, we employ a structure-sequence-aware disentangled multi-head attention mechanism (Figure S1C). This approach has been effectively used in several protein language models and has benefited from integrated multimodal information<sup>53–55</sup>. Specifically, let  $R \in \mathbb{R}^{N \times 128}$  denote the structure representation of a protein complex interface (with  $N$  residues), and let  $S, S_{\text{partner}} \in \mathbb{R}^{1 \times 128}$  be the sequence representation of the protein and its binding partner, respectively. To model cross-modality and cross-partner interactions between structure ( $r$ ) and sequence ( $s$ ) and binding partner sequence ( $sp$ ), we apply learnable linear projections to compute queries and keys as follows:

$$\begin{aligned} Q^r &= RW_r^q, K^r = RW_r^k, V^r = RW_r^v \\ Q^s &= SW_s^q, K^s = SW_s^k \\ Q^{sp} &= S_{\text{partner}}W_s^q, K^{sp} = S_{\text{partner}}W_s^k \end{aligned} \quad (3)$$

where  $W_r^q, W_r^k, W_r^v, W_s^q, W_s^k \in \mathbb{R}^{128 \times (8 \times 64)}$ . These projections produce 8 attention heads,



each with a dimensionality of 64. The projected tensors are then reshaped into the multi-head attention format:

$$\begin{aligned} Q^r, K^r, V^r &\in \mathbb{R}^{N \times 8 \times 64} \\ Q^s, K^s, Q^{sp}, K^{sp} &\in \mathbb{R}^{1 \times 8 \times 64} \end{aligned} \quad (4)$$

The cross-attention score  $A_i \in \mathbb{R}^{8 \times 64}$  for each residue  $i$  is computed as the sum of five directional attention terms:

$$\begin{aligned} A_i = & \underbrace{Q_i^r (K_i^r)^T}_{\text{(a) structure-to-structure}} + \underbrace{Q_i^r (K_i^s)^T}_{\text{(b) structure-to-sequence}} \\ & + \underbrace{Q_i^r (K_i^{sp})^T}_{\text{(c) structure-to-partner sequence}} + \underbrace{Q_i^s (K_i^r)^T}_{\text{(d) sequence-to-structure}} + \underbrace{Q_i^{sp} (K_i^r)^T}_{\text{(e) partner sequence-to-structure}} \end{aligned} \quad (5)$$

This design enables the structural representation to integrate information not only from itself, but also from both the intra-protein sequence and the binding partner's sequence, allowing comprehensive modeling of intra- and inter-protein interactions across both structural and sequence modalities. To stabilize training, the combined attention score is normalized by  $\sqrt{5d}$ , where  $d = 64$  is the head dimension. The final hidden state for residue  $i$  is:

$$H^{R_i} = FFN(\text{LayerNorm}(\text{softmax}(\frac{A_i}{\sqrt{5d}})V_{R_i})) + R_i \quad (6)$$

This updated hidden state is passed through a fully connected layer (size: 128), followed by another softmax layer, yielding a probability distribution for the 20 amino acid types for each residue in the protein complex (Figure 1A).

## Author contributions

Conceptualization: J.W. and J.L.; Methodology: J.W.; Validation: J.S., Y.Z., and H.Z.; Formal Analysis: J.W. and T.L.; Investigation: J.W., Y.Z., H.Z., and P.G.; Data Curation: J.W. and J.S.; Writing – Original Draft: J.W.; Writing – Review & Editing: T. Z., X.F., P.X. and J.L.; Supervision: J.L.; Project Administration: J.L.; Funding Acquisition: J.L.

## Conflict of interest

The authors declare no conflict of interest.

## Data and code availability



The pretrained DSSA-PPI model weights and preprocessed model input data can be found in <https://doi.org/10.5281/zenodo.15088340>. The data and codes that support the findings of this manuscript are openly available GitHub repository <https://github.com/Agitw/DSSA-PPI>.

### Acknowledgments

We gratefully acknowledge financial support from the Natural Science Foundation of China (22573016).



## References

View Article Online  
DOI: 10.1039/D5SC08898D

- (1) Lu, H.; Zhou, Q.; He, J.; Jiang, Z.; Peng, C.; Tong, R.; Shi, J. Recent Advances in the Development of Protein–Protein Interactions Modulators: Mechanisms and Clinical Trials. *Signal Transduct. Target. Ther.* **2020**, *5*, 213.
- (2) Qian, X.; Zhao, X.; Yu, L.; Yin, Y.; Zhang, X.-D.; Wang, L.; Li, J.-X.; Zhu, Q.; Luo, J.-L. Current Status of GABA Receptor Subtypes in Analgesia. *Biomed. Pharmacother.* **2023**, *168*, 115800.
- (3) Tuller, T.; Atar, S.; Ruppin, E.; Gurevich, M.; Achiron, A. Common and Specific Signatures of Gene Expression and Protein–Protein Interactions in Autoimmune Diseases. *Genes Immun.* **2013**, *14*, 67–82.
- (4) Hong, H.; Su, J.; Zhang, Y.; Xu, G.; Huang, C.; Bao, G.; Cui, Z. A Novel Role of Lactate: Promotion of Akt-Dependent Elongation of Microglial Process. *Int. Immunopharmacol.* **2023**, *119*, 110136.
- (5) Humphrey, S. J.; James, D. E.; Mann, M. Protein Phosphorylation: A Major Switch Mechanism for Metabolic Regulation. *Trends Endocrinol. Metab.* **2015**, *26*, 676–687.
- (6) Wu, J.; Shi, Y.; Zhou, M.; Chen, M.; Ji, S.; Liu, X.; Zhou, M.; Xia, R.; Zheng, X.; Wang, W. Nutrient Vitamins Enabled Metabolic Regulation of Ferroptosis via Reactive Oxygen Species Biology. *Front. Pharmacol.* **2024**, *15*, 1434088.
- (7) Petrosino, M.; Novak, L.; Pasquo, A.; Chiaraluce, R.; Turina, P.; Capriotti, E.; Consalvi, V. Analysis and Interpretation of the Impact of Missense Variants in Cancer. *Int. J. Mol. Sci.* **2021**, *22*, 5416.
- (8) Song, F.; Lu, C.-L.; Wang, C.-G.; Hu, C.-W.; Zhang, Y.; Wang, T.-L.; Han, L.; Chen, Z. Uncovering the Mechanism of Kang-Ai Injection for Treating Intrahepatic Cholangiocarcinoma Based on Network Pharmacology, Molecular Docking, and in Vitro Validation. *Front. Pharmacol.* **2023**, *14*, 1129709.
- (9) Zhao, J.; Ma, J.; Deng, Y.; Kelly, J. A.; Kim, K.; Bang, S.-Y.; Lee, H.-S.; Li, Q.-Z.; Wakeland, E. K.; Qiu, R. A Missense Variant in NCF1 Is Associated with Susceptibility to Multiple Autoimmune Diseases. *Nat. Genet.* **2017**, *49*, 433–437.
- (10) Qin, Y.; Chen, L.; Fei, Q.; Shao, X.; Lv, W.; Yang, J.; Xu, F.; Shi, J. Upregulation of CD226 on Subsets of T Cells and NK Cells Is Associated with Upregulated Adhesion Molecules and Cytotoxic Factors in Patients with Tuberculosis. *Int. Immunopharmacol.* **2023**, *120*, 110360.
- (11) Geisheker, M. R.; Heymann, G.; Wang, T.; Coe, B. P.; Turner, T. N.; Stessman, H. A.; Hoekzema, K.; Kvarnung, M.; Shaw, M.; Friend, K. Hotspots of Missense Mutation Identify Neurodevelopmental Disorder Genes and Functional Domains. *Nat. Neurosci.* **2017**, *20*, 1043–1051.
- (12) Hu, Z.; Gu, Y.; Ye, M.; Ma, Y.; Wang, Y.; Pan, S.; Huang, C.; Lu, X. Innate Immune Stimulation Prevents Chronic Stress-Induced Depressive and Anxiogenic-like Behaviors in Female Mice. *Int. Immunopharmacol.* **2022**, *111*, 109126.
- (13) Fowler, D. M.; Fields, S. Deep Mutational Scanning: A New Style of Protein Science. *Nat. Methods* **2014**, *11*, 801–807.
- (14) Schymkowitz, J.; Borg, J.; Stricher, F.; Nys, R.; Rousseau, F.; Serrano, L. The FoldX Web Server: An Online Force Field. *Nucleic Acids Res.* **2005**, *33*, W382–W388.
- (15) Barlow, K. A.; Ó Conchúir, S.; Thompson, S.; Suresh, P.; Lucas, J. E.; Heinonen, M.;





- Kortemme, T. Flex ddG: Rosetta Ensemble-Based Estimation of Changes in Protein-Protein Binding Affinity upon Mutation. *J. Phys. Chem. B* **2018**, *122*, 5389–5399.
- (16) Xie, S.; Zhou, Y.; Zhu, H.; Xu, X.; Zhang, H.; Yuan, C.; Huang, M.; Xu, P.; Li, J.; Liu, Y. Interface-Driven Structural Evolution on Diltiazem as Novel uPAR Inhibitors: From in Silico Design to in Vitro Evaluation. *Mol. Divers.* **2025**, *29*, 1261–1274.
- (17) Wang, E.; Sun, H.; Wang, J.; Wang, Z.; Liu, H.; Zhang, J. Z. H.; Hou, T. End-Point Binding Free Energy Calculation with MM/PBSA and MM/GBSA: Strategies and Applications in Drug Design. *Chem. Rev.* **2019**, *119*, 9478–9508.
- (18) Li, G.; Pahari, S.; Murthy, A. K.; Liang, S.; Fragoza, R.; Yu, H.; Alexov, E. SAAMBE-SEQ: A Sequence-Based Method for Predicting Mutation Effect on Protein-Protein Binding Affinity. *Bioinformatics* **2021**, *37*, 992–999.
- (19) Abbasi, W. A.; Yaseen, A.; Hassan, F. U.; Andleeb, S.; Minhas, F. U. A. A. ISLAND: In-Silico Proteins Binding Affinity Prediction Using Sequence Information. *BioData Min.* **2020**, *13*, 1–13.
- (20) Wang, M.; Cang, Z.; Wei, G.-W. A Topology-Based Network Tree for the Prediction of Protein-Protein Binding Affinity Changes Following Mutation. *Nat. Mach. Intell.* **2020**, *2*, 116–123.
- (21) Wee, J.; Wei, G.-W. Evaluation of AlphaFold 3's Protein-Protein Complexes for Predicting Binding Free Energy Changes upon Mutation. *J. Chem. Inf. Model.* **2024**, *64*, 6676–6683.
- (22) Liu, X.; Luo, Y.; Li, P.; Song, S.; Peng, J. Deep Geometric Representations for Modeling Effects of Mutations on Protein-Protein Binding Affinity. *PLOS Comput. Biol.* **2021**, *17*, e1009284.
- (23) Yue, Y.; Li, S.; Wang, L.; Liu, H.; Tong, H. H. Y.; He, S. MpbPPI: A Multi-Task Pre-Training-Based Equivariant Approach for the Prediction of the Effect of Amino Acid Mutations on Protein-Protein Interactions. *Brief. Bioinform.* **2023**, *24*, bbad310.
- (24) Li, P.; Liu, Z.-P. MuToN Quantifies Binding Affinity Changes upon Protein Mutations by Geometric Deep Learning. *Adv. Sci.* **2024**, *11*, 2402918.
- (25) Jumper, J.; Evans, R.; Pritzel, A.; Green, T.; Figurnov, M.; Ronneberger, O.; Tunyasuvunakool, K.; Bates, R.; Žídek, A.; Potapenko, A. Highly Accurate Protein Structure Prediction with AlphaFold. *Nature* **2021**, *596*, 583–589.
- (26) Baek, M.; DiMaio, F.; Anishchenko, I.; Dauparas, J.; Ovchinnikov, S.; Lee, G. R.; Wang, J.; Cong, Q.; Kinch, L. N.; Schaeffer, R. D. Accurate Prediction of Protein Structures and Interactions Using a Three-Track Neural Network. *Science* **2021**, *373*, 871–876.
- (27) Raouraoua, N.; Mirabello, C.; Véry, T.; Blanchet, C.; Wallner, B.; Lensink, M. F.; Brysbaert, G. MassiveFold: Unveiling AlphaFold's Hidden Potential with Optimized and Parallelized Massive Sampling. *Nat. Comput. Sci.* **2024**, 1–5.
- (28) Kilim, O.; Mentés, A.; Pál, B.; Csabai, I.; Gellért, Á. SARS-CoV-2 Receptor-Binding Domain Deep Mutational AlphaFold2 Structures. *Sci. Data* **2023**, *10*, 134.
- (29) Bushuiev, A.; Bushuiev, R.; Kouba, P.; Filkin, A.; Gabrielova, M.; Gabriel, M.; Sedlar, J.; Pluskal, T.; Damborsky, J.; Mazurenko, S.; Sivic, J. Learning to Design Protein-Protein Interactions with Enhanced Generalization. *ICLR* **2024**, <https://openreview.net/forum?id=xcMmehCT7s>.



- (30) Jemimah, S.; Sekijima, M.; Gromiha, M. M. ProAffiMuSeq: Sequence-Based Method to Predict the Binding Free Energy Change of Protein–Protein Complexes upon Mutation Using Functional Classification. *Bioinformatics* **2020**, *36*, 1725–1730.
- (31) Gurusinghe, S. N. S.; Wu, Y.; DeGrado, W.; Shifman, J. M. ProBASS—a Language Model with Sequence and Structural Features for Predicting the Effect of Mutations on Binding Affinity. *Bioinformatics* **2025**, *41*, btaf270.
- (32) Liao, Y.-L.; Smidt, T. Equiformer: Equivariant Graph Attention Transformer for 3D Atomistic Graphs. *ICLR* **2023**, <https://openreview.net/forum?id=KwmPfARgOTD>.
- (33) Kellogg, E. H.; Leaver-Fay, A.; Baker, D. Role of Conformational Sampling in Computing Mutation-Induced Changes in Protein Structure and Stability. *Proteins Struct. Funct. Bioinforma.* **2011**, *79*, 830–838.
- (34) Manson, A.; Whitten, S. T.; Ferreon, J. C.; Fox, R. O.; Hilser, V. J. Characterizing the Role of Ensemble Modulation in Mutation-Induced Changes in Binding Affinity. *J. Am. Chem. Soc.* **2009**, *131*, 6785–6793.
- (35) Verkhivker, G.; Agajanian, S.; Oztas, D.; Gupta, G. Dynamic Profiling of Binding and Allosteric Propensities of the SARS-CoV-2 Spike Protein with Different Classes of Antibodies: Mutational and Perturbation-Based Scanning Reveals the Allosteric Duality of Functionally Adaptable Hotspots. *J. Chem. Theory Comput.* **2021**, *17*, 4578–4598.
- (36) Atilgan, A. R.; Durell, S. R.; Jernigan, R. L.; Demirel, M. C.; Keskin, O.; Bahar, I. Anisotropy of Fluctuation Dynamics of Proteins with an Elastic Network Model. *Biophys. J.* **2001**, *80*, 505–515.
- (37) Lewis, S.; Hempel, T.; Jiménez-Luna, J.; Gastegger, M.; Xie, Y.; Foong, A. Y. K.; Satorras, V. G.; Abidin, O.; Veeling, B. S.; Zaporozhets, I.; Chen, Y.; Yang, S.; Foster, A. E.; Schneuing, A.; Nigam, J.; Barbero, F.; Stimper, V.; Campbell, A.; Yim, J.; Lienen, M.; Shi, Y.; Zheng, S.; Schulz, H.; Munir, U.; Sordillo, R.; Tomioka, R.; Clementi, C.; Noé, F. Scalable Emulation of Protein Equilibrium Ensembles with Generative Deep Learning. *Science* **2025**, *389*, eadv9817.
- (38) Charron, N. E.; Bonneau, K.; Pasos-Trejo, A. S.; Guljas, A.; Chen, Y.; Musil, F.; Venturin, J.; Gusew, D.; Zaporozhets, I.; Krämer, A.; Templeton, C.; Kelkar, A.; Durumeric, A. E. P.; Olsson, S.; Pérez, A.; Majewski, M.; Husic, B. E.; Patel, A.; De Fabritiis, G.; Noé, F.; Clementi, C. Navigating Protein Landscapes with a Machine-Learned Transferable Coarse-Grained Model. *Nat. Chem.* **2025**, *17*, 1284–1292.
- (39) Jin, Y.; Huang, Q.; Song, Z.; Zheng, M.; Teng, D.; Shi, Q. P2DFlow: A Protein Ensemble Generative Model with SE(3) Flow Matching. *J. Chem. Theory Comput.* **2025**, *21*, 3288–3296.
- (40) Tsishyn, M.; Pucci, F.; Rومان, M. Quantification of Biases in Predictions of Protein–Protein Binding Affinity Changes upon Mutations. *Brief. Bioinform.* **2024**, *25*, bbad491.
- (41) Zhang, R.; Chen, N.; Zhou, F.; Gao, X. Navigating Trustworthiness of Deep Learning in  $\Delta\Delta G$  Prediction : Addressing Data Bias, Model Evaluation, and Interpretation. In *ICML 2024 Workshop on Machine Learning for Life and Material Science* **2024**, <https://openreview.net/forum?id=XU1ACMwTlr>.
- (42) Chi, L. A.; Barnes, J. E.; Patel, J. S.; Ytreberg, F. M. Exploring the Ability of the MD+FoldX Method to Predict SARS-CoV-2 Antibody Escape Mutations Using Large-



- Scale Data. *Sci. Rep.* **2024**, *14*, 23122.
- (43) Wee, J.; Chen, J.; Xia, K.; Wei, G.-W. Integration of Persistent Laplacian and Pre-Trained Transformer for Protein Solubility Changes upon Mutation. *Comput. Biol. Med.* **2024**, *169*, 107918.
- (44) Starr, T. N.; Greaney, A. J.; Hilton, S. K.; Ellis, D.; Crawford, K. H. D.; Dingens, A. S.; Navarro, M. J.; Bowen, J. E.; Tortorici, M. A.; Walls, A. C.; King, N. P.; Velesler, D.; Bloom, J. D. Deep Mutational Scanning of SARS-CoV-2 Receptor Binding Domain Reveals Constraints on Folding and ACE2 Binding. *Cell* **2020**, *182*, 1295-1310.e20.
- (45) Pondé, R. A. A. Physicochemical Effect of the N501Y, E484K/Q, K417N/T, L452R and T478K Mutations on the SARS-CoV-2 Spike Protein RBD and Its Influence on Agent Fitness and on Attributes Developed by Emerging Variants of Concern. *Virology* **2022**, *572*, 44–54.
- (46) Lan, J.; He, X.; Ren, Y.; Wang, Z.; Zhou, H.; Fan, S.; Zhu, C.; Liu, D.; Shao, B.; Liu, T.-Y.; Wang, Q.; Zhang, L.; Ge, J.; Wang, T.; Wang, X. Structural Insights into the SARS-CoV-2 Omicron RBD-ACE2 Interaction. *Cell Res.* **2022**, *32*, 593–595.
- (47) Zhou, Y.; Wang, D.; Wu, J.; Qi, Y.; Song, M.; Yao, H.; Liao, C. K.; Lin, H.; Huang, M.; Zhuo, D.; Jiang, L.; Yuan, C.; Chen, Y.; Huang, M.; Li, J.; Xu, P. Discovery of the Low-Hemorrhagic Antithrombotic Effect of Montelukast by Targeting FXIa in Mice. *Arterioscler. Thromb. Vasc. Biol.* **2025**, *45*, e150–e162.
- (48) Koulas, I.; Spyropoulos, A. C. A Review of FXIa Inhibition as a Novel Target for Anticoagulation. *Hämostaseologie* **2023**, *43*, 028–036.
- (49) Andersen, L. M.; Wind, T.; Hansen, H. D.; Andreasen, P. A. A Cyclic Peptidyl Inhibitor of Murine Urokinase-Type Plasminogen Activator: Changing Species Specificity by Substitution of a Single Residue. *Biochem. J.* **2008**, *412*, 447–457.
- (50) Xu, P.; Xu, M.; Jiang, L.; Yang, Q.; Luo, Z.; Dauter, Z.; Huang, M.; Andreasen, P. A. Design of Specific Serine Protease Inhibitors Based on a Versatile Peptide Scaffold: Conversion of a Urokinase Inhibitor to a Plasma Kallikrein Inhibitor. *J. Med. Chem.* **2015**, *58*, 8868–8876.
- (51) Zhao, B.; Xu, P.; Jiang, L.; Paaske, B.; Kromann-Hansen, T.; Jensen, J. K.; Sørensen, H. P.; Liu, Z.; Nielsen, J. T.; Christensen, A.; Hosseini, M.; Sørensen, K. K.; Nielsen, N. C.; Jensen, K. J.; Huang, M.; Andreasen, P. A. A Cyclic Peptidic Serine Protease Inhibitor: Increasing Affinity by Increasing Peptide Flexibility. *PLoS ONE* **2014**, *9*, e115872.
- (52) Dauparas, J.; Anishchenko, I.; Bennett, N.; Bai, H.; Ragotte, R. J.; Milles, L. F.; Wicky, B. I. M.; Courbet, A.; de Haas, R. J.; Bethel, N.; Leung, P. J. Y.; Huddy, T. F.; Pellock, S.; Tischer, D.; Chan, F.; Koepnick, B.; Nguyen, H.; Kang, A.; Sankaran, B.; Bera, A. K.; King, N. P.; Baker, D. Robust Deep Learning-Based Protein Sequence Design Using ProteinMPNN. *Science* **2022**, *378*, 49–56.
- (53) Tan, Y.; Wang, R.; Wu, B.; Hong, L.; Zhou, B. Retrieval-Enhanced Mutation Mastery: Augmenting Zero-Shot Prediction of Protein Language Model. *arXiv:2410.21127* **2024**, <https://doi.org/10.48550/arXiv.2410.21127>.
- (54) Wang, D.; Pourmirzaei, M.; Abbas, U. L.; Zeng, S.; Manshour, N.; Esmaili, F.; Poudel, B.; Jiang, Y.; Shao, Q.; Chen, J. S-PLM: Structure-Aware Protein Language Model via Contrastive Learning Between Sequence and Structure. *Adv. Sci.* **2025**, *12*,



2404212.

[View Article Online](#)  
DOI: 10.1039/D5SC08898D

- (55) Li, M.; Tan, Y.; Ma, X.; Zhong, B.; Yu, H.; Zhou, Z.; Ouyang, W.; Zhou, B.; Tan, P.; Hong, L. ProSST: Protein Language Modeling with Quantized Structure and Disentangled Attention. *NeurIPS* **2024**, DOI: 10.52202/079017-1126.



The pretrained DSSA-PPI model weights and preprocessed model input data can be found in <https://doi.org/10.5281/zenodo.15088340>. The data and codes that support the findings of this manuscript are openly available GitHub repository <https://github.com/Agitw/DSSA-PPI>.

